Origins of oblique-slip faulting during caldera subsidence

Eoghan P. Holohan,[1,2] Thomas R. Walter,[2] Martin P.J. Schöpfer,[1,3] John J. Walsh,[1] Benjamin van Wyk de Vries,[4] and Valentin R. Troll[5]

Received 21 June 2012; revised 27 November 2012; accepted 11 December 2012.

[1] Although conventionally described as purely dip-slip, faults at caldera volcanoes may have a strike-slip displacement component. Examples occur in the calderas of Olympus Mons (Mars), Miyakejima (Japan), and Dolomieu (La Reunion). To investigate this phenomenon, we use numerical and analog simulations of caldera subsidence caused by magma reservoir deflation. The numerical models constrain mechanical causes of oblique-slip faulting from the three-dimensional stress field in the initial elastic phase of subsidence. The analog experiments directly characterize the development of oblique-slip faulting, especially in the later, non-elastic phases of subsidence. The combined results of both approaches can account for the orientation, mode, and location of oblique-slip faulting at natural calderas. Kinematically, oblique-slip faulting originates to resolve the following: (1) horizontal components of displacement that are directed radially toward the caldera center and (2) horizontal translation arising from off-centered or "asymmetric" subsidence. We informally call these two origins the "camera iris" and "sliding trapdoor" effects, respectively. Our findings emphasize the fundamentally three-dimensional nature of deformation during caldera subsidence. They hence provide an improved basis for analyzing structural, geodetic, and geophysical data from calderas, as well as analogous systems, such as mines and producing hydrocarbon reservoirs.

Citation: Holohan, E. P., T. R. Walter, M. P. J. Schöpfer, J. J. Walsh, B. van Wyk de Vries, and V. R. Troll (2013), Origins of oblique-slip faulting during caldera subsidence, *J. Geophys. Res. Solid Earth*, *118*, doi:10.1002/jgrb.50057.

1. Introduction

[2] Calderas are km-scale topographic depressions found in all volcanic settings on Earth [*Geyer and Marti*, 2008] and in almost every volcanic region of the Solar System [*Crumpler et al*., 1996]. They form when depletion of a subsurface magma reservoir leads to subsidence of the reservoir roof. Caldera subsidence can occur at rates of several tens to several hundreds of meters per day [*Geshi et al*., 2002; *Wilson and Hildreth*, 1997] and in conjunction with voluminous eruptions, large earthquakes [*Stix and Kobayashi*, 2008], or even tsunamis [*Latter*, 1981]. Despite such hazards, caldera volcanoes can be economically beneficial sources of geothermal energy and minerals [*Rytuba*, 1994].

[3] Within a wider context, caldera formation is one of several subsidence processes driven by depletion of material from a subsurface body. Man-made examples are commonly caused by mining, ground-water pumping, or hydrocarbon extraction. Gross similarity between natural and man-made subsidence means that insights into one process are often transferable to the others [*Branney*, 1995; *Odonne et al*., 1999].

[4] One unresolved problem in the structural accommodation of caldera subsidence is the occurrence of faults with a strike-slip displacement component. Although previous field-based, experimental, or numerical studies typically describe or consider caldera subsidence faults as purely dip-slip structures, we highlight remote sensing and field and geophysical evidence for oblique slip (section 2). Current characterizations of the geometry and development of caldera fracture systems, as well as explanations of how stress conditions during subsidence lead to such fractures are therefore incomplete.

[5] To explain the mechanical and kinematic origins of oblique-slip faulting at calderas, we develop upon *Sanford*'s [1959] approach (section 3) and compare structural predictions from continuum-based numerical models (section 4) with structural observations from scaled analog experiments (section 5). Importantly, we consider the problem in three dimensions rather than two. We then discuss how this combined approach can help to account for the orientation, mode, and location of oblique-slip faulting in natural calderas (section 6). We also discuss some geophysical implications of our results.

All supporting information may be found in the online version of this article.

[1]Fault Analysis Group, UCD School of Geological Sciences, University College Dublin, Dublin 4, Ireland.
[2]Helmholtz Centre Potsdam, German Research Centre for Geosciences (GFZ), Section 2.1, Telegrafenberg, Potsdam, Germany.
[3]Department for Geodynamics and Sedimentology, University of Vienna, Vienna, Austria.
[4]Laboratoire Magmas et Volcans, 5 rue Kessler, 63038 Clermont-Ferrand, France.
[5]Department of Earth Sciences, CEMPEG, Uppsala University, Uppsala, Sweden.

Corresponding author: E. P. Holohan, Helmholtz Centre Potsdam, German Research Centre for Geosciences (GFZ), Section 2.1, Telegrafenberg, Potsdam 14473, Germany. (holohan@gfz-potsdam.de)

2169-9313/13/10.1002/jgrb.50057

2. Oblique-slip Faulting at Calderas in Nature

2.1. Context

[6] Past studies show that subsidence-related deformation is characterized by a central zone of horizontal contraction and a peripheral zone of horizontal extension [*Branney*, 1995; *Marti et al*., 1994; *Roche et al*., 2000; *Walter and Troll*, 2001; *Zuber and Mouginis-Mark*, 1992]. Correspondingly, a two-zone distribution of caldera structures is commonly seen in map view and cross-section.

[7] Central zone structures may include the following:

[8] (1) A centroclinal "down-sag" of the caldera floor [*Branney*, 1995; *Moore and Kokelaar*, 1998; *Walker*, 1984].

[9] (2) Thrust-related wrinkle ridges [*Plescia and Golombek*, 1986] that trend radially or concentrically with respect to the caldera center [*Mouginis-Mark and Robinson*, 1992].

[10] (3) Arcuate or ring-like faults with a reverse sense of slip and an outward dip with respect to the caldera center [*Anderson*, 1936; *Clough et al*., 1909; *Mori and Mckee*, 1987].

[11] Peripheral zone structures may include the following:

[12] (1) Tensile fractures, fissures, or crevasse that strike concentrically to the caldera center [*Michon et al*., 2009; *Moore and Kokelaar*, 1998].

[13] (2) Minor normal faults that strike concentrically to the caldera center and dip either inward or outward. These delimit horsts, grabens, "step-fault" blocks, and/or marginal benches [*Branney*, 1995; *Kennedy et al*., 2004].

[14] (3) Major arcuate or ring-like faults with a normal sense of slip and an inward dip with respect to the caldera center [*Lipman*, 1997].

[15] The subsidence-related fractures described or considered in such past studies are purely dip-slip (i.e., reverse or normal faults) or opening mode (tensile fractures or fissures). At some exceptionally well-exposed or well-monitored calderas, however, evidence exists that subsidence-related faults may also have a strike-slip displacement component.

2.2. Evidence

2.2.1. Olympus Mons

[16] Olympus Mons caldera (Figure 1a) is a 60 km diameter depression at the summit of the largest volcanic edifice in the Solar System. Published maps [*Mouginis-Mark and Robinson*, 1992] show that the caldera's central zone displays a down-sagged surface and numerous wrinkle ridges. The peripheral zone displays a network of intersecting fault sets that delimit horsts and grabens. It also displays a 2 km high concentric fault scarp, set into which are numerous "step-faults." In a transitional position between the central and peripheral zones, "concentric ridges" offset other features in an apparent strike-slip manner [*Zuber and Mouginis-Mark*, 1992].

[17] Upon re-examining these "concentric ridges" in the published image (Figure 1a), we noted a lack of shadow on the side facing away from the illumination source. This indicates a step-like morphology, rather than a true ridge and is compatible with the scarp of a fault down-throwing toward the caldera center. The "concentric ridges" hence display both dip-slip and strike-slip displacement components—i.e., they are the traces of oblique-slip faults. We show below that our models reproduce the transitional position and slip-sense of these faults.

2.2.2. Miyakejima

[18] Miyakejima caldera (Figure 1b) is a 1.6 km diameter depression at the summit of a basaltic-andesitic volcano in the Izu-Bonin island arc, south of Japan. In July 2000, lateral propagation of a dyke from a reservoir deep below the volcano triggered a major collapse event [*Toda et al*., 2002]. A consequent lack of eruption clouds at the caldera enabled the capture of aerial photographs during the collapse's earliest stages. Analysis of near-surface structures and ground displacements revealed a central zone delimited by a reverse ring fault and a peripheral zone delimited by a normal ring fault [*Geshi et al*., 2002]. Upon a closer examination of the aerial photo sequence, we noted additional complexity to the caldera's structural development, including evidence for oblique-slip faulting.

[19] Firstly, along the northwestern side of the caldera, the outer normal ring fault only formed fully after the sequential displacement of a number of marginal blocks (Figure 1b). A main marginal block ("B1" in Figure 1b) formed initially, after which two smaller marginal blocks ("B2" and "B3" in Figure 1b) detached to establish new segments of the outer normal ring fault. Horizontal displacement vectors [*Geshi et al*., 2002] at either end of the main marginal block are directed obliquely to the adjacent fault scarp segments, and so indicate oblique-slip here. We show below that this sequential marginal block development, associated with oblique-slip faulting, is compatible with a relatively thick and horizontally elongated reservoir roof.

[20] Secondly, the height of the inner ring fault scarp decreases systematically from the NE to the SW, where there is a series of small, sharply defined normal fault scarps. This is suggestive of a central block that is tilted in trapdoor fashion toward the NE, with an extensional "hinge" in the SW. The one horizontal displacement vector defined in the nonsagged central zone [*Geshi et al*., 2002] could be interpreted, albeit tentatively, as evidence for the central block's initial NE-ward displacement, i.e., toward the area of maximum subsidence. We show below that this structure and displacement of the central zone is compatible with oblique-slip on the inner ring fault, as developed by "trapdoor-like" subsidence.

2.2.3. Dolomieu

[21] Dolomieu crater (Figure 1c) is a 1 km diameter depression at the summit of the basaltic Piton de la Fournaise volcano, La Reunion. In April 2007, as at Miyakejima, Dolomieu collapsed as a result of a lateral dyke intrusion [*Staudacher et al*., 2009]. Inside the caldera, a steeply inward-inclined normal ring fault was observed to enclose several marginal benches [*Michon et al*., 2009]. Horizontal displacement vectors measured outside the caldera by GPS [*Michon et al*., 2009] show a radially inward-directed pattern with magnitudes of up to 2.2 m during the collapse itself and up to 40 cm during post-collapse deflation (Figure 1c).

[22] Syn- and post-collapse earthquake source mechanisms were characterized [*Massin et al*., 2011] either as non-double couple and indicative of horizontal contraction or as double couple and indicative of horizontal extension with a weak to strong rake—i.e., oblique-normal to strike-slip faults (Figure 1c). As we discuss below, our models provide several insights into the potential origins of both types of these earthquakes.

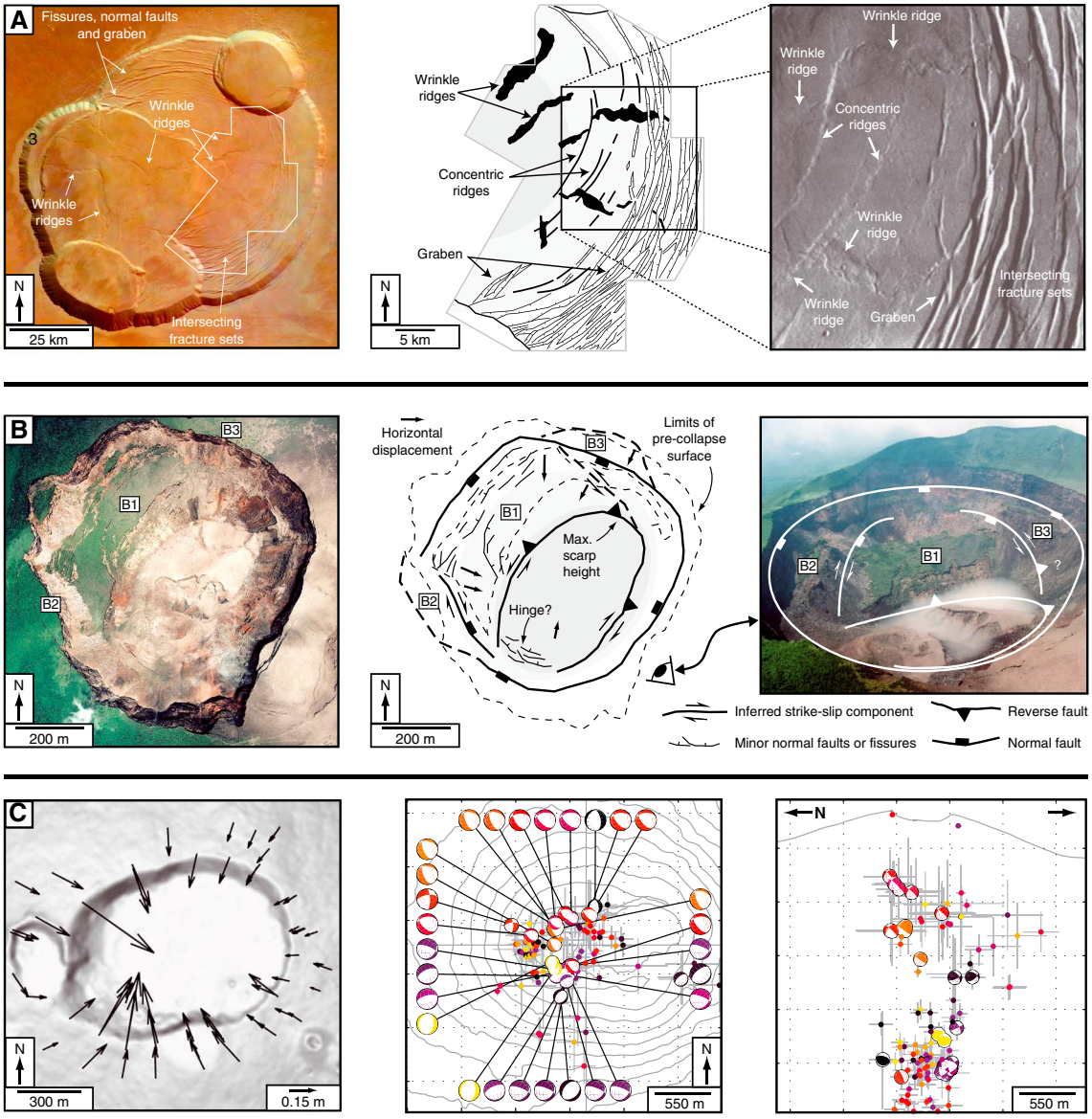

Figure 1. Evidence of oblique-slip faulting at natural calderas. (a) Olympus Mons Caldera, Mars. Left: ESA Mars Express image with some main structures noted (illumination from the southeast); center: structural map of area outlined in left image (redrawn from *Zuber and Mouginis-Mark* [1992]); right: Viking Orbiter image (from *Zuber and Mouginis-Mark* [1992]) of the area boxed in center image. Enigmatic "concentric ridges" show evidence for strike-slip and dip-slip displacement components. (b) Miyakejima caldera, Japan. Left: plan-view photo taken on 09 July 2000, shortly after onset of collapse (image by Asia Air Survey Co. Ltd); center: map of structures and horizontal displacements observed during collapse (data from *Geshi et al.* [2002]); right: the caldera on 11 July 2000 after further subsidence (image by H. Murakami). All strike-slip components of fault motion are interpretations from this study. (c) Dolomieu caldera, La Reunion Island. Left: shaded relief map showing subsidence-related horizontal displacements during May–November 2007 [*Michon et al.*, 2009]; center: earthquake focal mechanisms (double couple = spheres; non-double couple = points) during subsidence from April to end of May 2007 [*Massin et al.*, 2011]; right: depth distribution of the focal mechanisms [*Massin et al.*, 2011]. Note the abundance of oblique-slip events.

3. Methods

[23] Continuum-based numerical modeling is commonly used to provide insight into the mechanics of subsidence-related faulting. Such modeling facilitates the calculation of the stress-field generated around a source of deformation within a medium that has rock-like material properties. The locations, orientations, and modes of potential fractures are estimated by comparing the orientation and magnitude of calculated stresses to an appropriate failure criterion [cf. *Sanford*, 1959]. Unlike discontinuum-based numerical modeling or analog experiments, a continuum-based approach without plasticity is unable to directly simulate fracture development. Therefore, some caution must be exercised when attempting to use this

approach to simulate a highly discontinuous (i.e., fracture-dominated) deformation process such as caldera subsidence, especially in its advanced stages. A continuum-based approach nonetheless offers the advantage of a speedy, first-order prediction of fracturing in the preliminary stages of a brittle deformation process and a rapid exploration of the initial effects of various mechanical and geometric factors.

[24] Scaled analog modeling can overcome the limitations of continuum-based numerical models and can independently test their predictions. However, the scaling of analog model structures, material properties, and deformation timescales to those in nature is not as precise. Nonetheless, the technique can provide very instructive qualitative insights into the three-dimensional geometry and kinematic development of caldera structures, as shown by the striking similarities of past analog model results to natural structures.

3.1. Numerical Subsidence Models

3.1.1. Stresses From Magma Reservoir Deflation

[25] The stress field related to magma reservoir deflation was calculated by using the Boundary Element Method (BEM) modeling software Poly3D [*Thomas*, 1993]. This open-source software calculates displacements, strains, and stresses in an isotropic elastic full- or half-space subjected to connected triangular elements of dislocation (for theory, see [*Jeyakumaran et al.*, 1992]). The upper boundary of the model was subject to a half-space condition, while the lateral and lower boundaries were at infinity (Figure 2). To represent a magma reservoir's finite boundary, we created a spheroidal mesh of elements. Deflation of a magma reservoir due to magma withdrawal was simulated by imposing an inward-directed pressure normal to each element of the model reservoir boundary. We chose to model a 10 km diameter, sill-like magma reservoir (oblate ellipsoid) located at a depth of 2, 4, or 8 km.

[26] Although the models were fully three-dimensional, the oblate reservoir shape meant that principal stress components orientated non-perpendicular or non-parallel to any vertical plane of section passing radially through the reservoir center were extremely small (unit vector length <0.005). Consequently, the results were treated for visualization purposes as effectively axi-symmetric—i.e., we fixed two of the three principal stresses to lie in the plane of cross-section, with the other lying perpendicular to that plane.

3.1.2. Superposition Upon a Gravitational Stress Field

[27] Reservoir deflation stresses were then superimposed, within the same coordinate system, upon a reference gravitational stress field [cf. *Sanford*, 1959; *Twiss and Moores*, 1992]. At each point, the resultant stress tensor's eigenvectors and eigenvalues yielded new principal stress orientations and magnitudes, respectively. For each equivalent point of the elastic medium, we assumed the gravitational stress states to have a vertical maximum principal stress (σ_1) with horizontal intermediate (σ_2) and minimum (σ_3) principal stresses. The magnitudes of these principal stresses are given by:

$$\sigma_1 = \rho g z \tag{1}$$

and

$$\sigma_2 = \sigma_3 = k \rho g z \tag{2}$$

where z is the depth below the Earth's surface, ρ is the rock mass density, g is gravitational acceleration (Table 1). The constant k accounts for the effect of Poisson's ratio v and is given by [*Twiss and Moores*, 1992]:

$$k = v/(1 - v) \tag{3}$$

3.1.3. Predicting the Location, Mode, and Orientation of Initial Fractures

[28] To predict regions of material failure, the resultant principal stress magnitudes were compared to a *Paul* [1961] failure criterion (Figure 3). The Paul criterion is very similar to the widely used *Anderson* [1951] fracture theory, but is mathematically more rigorous. In the compressive field, the Paul criterion comprises a linear Mohr-Coulomb

Table 1. Material Parameters Used to Calculate Stress Fields and Failure Regions

Symbol	Parameter	Value	Units
E	Young's modulus	50	GPa
v	Poisson's ratio	0.35	-
g	Gravitational acceleration	9.81	ms^{-2}
ρ	Density	2700	kgm^{-3}
UCS	Unconfined compressive strength	17.3	MPa
UTS	Unconfined tensile strength	−2.8	MPa
C	Cohesion	5	MPa
φ	Friction angle	30	deg

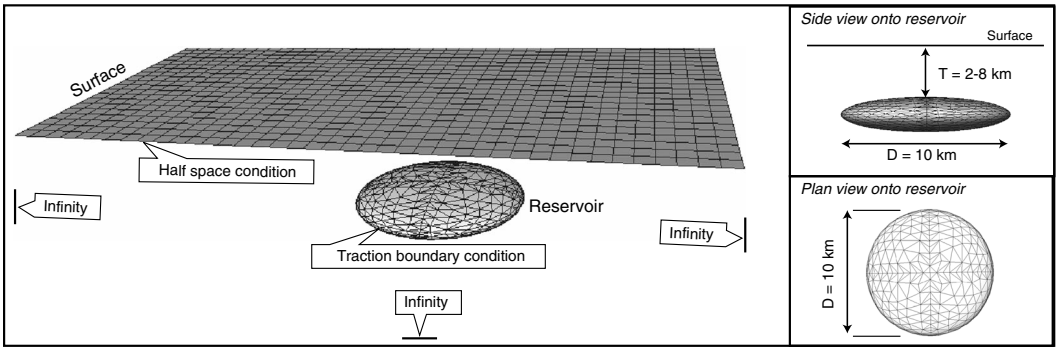

Figure 2. Perspective view and boundary conditions of Boundary Element Method (BEM) model for magma reservoir deflation. Insets show modeled reservoir dimensions.

failure envelope. In the tensile field, where Anderson's theory is undefined, it combines this linear envelope with a vertical tensile cutoff, thereby approximating the parabolic shape typical of laboratory-derived rock failure envelopes (Figure 3).

[29] The Paul criterion, like Anderson's theory, considers two end-member modes of fracture: shear and tensile. Shear fracture is assumed if the normal stress on a potential shear failure plane is compressive, whereas tensile fracture is assumed if it this stress tensile. On this basis, the shear to tensile transition is the point on the linear envelope where σ_1 equals half the material's unconfined compressive strength (UCS) (Figure 3a). The value of σ_3 at this point corresponds to the material's unconfined tensile strength (UTS).

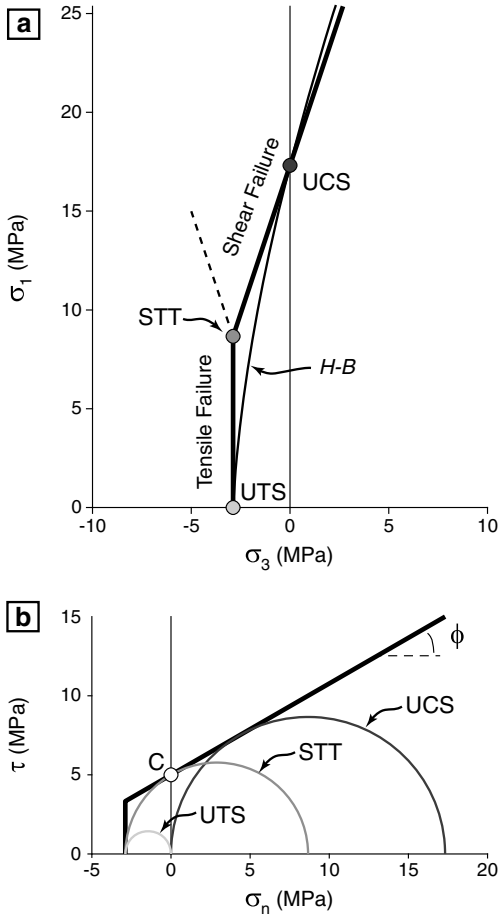

Figure 3. The Paul failure criterion as used in this study. (a) Paul criterion (thick black line) plotted in principal stress space. The criterion is defined by the unconfined compressive strength (UCS), unconfined tensile strength (UTS), and the shear to tensile transition (STT). The dashed line joins the STT points of Paul criteria for all possible cohesions. It thus separates shear and tensile failure for stress states exceeding the criterion in the elastic medium. For comparison with curved envelopes typical of laboratory test data, a thin line marked H-B shows a Hoek-Brown criterion plotted for the same values of UCS and UTS. (b) Paul criterion (thick black line) plotted in Mohr space. This shows the relationship of the criterion to material cohesion (C) and angle of internal friction (ϕ).

Since UCS and UTS are proportional to the material's cohesion, the Paul criterion may be fully defined by values for cohesion and the material's angle of internal friction [cf. *Jaeger et al*., 2007] (Figure 3b).

[30] For shear fracture, two conjugate failure planes form with the acute angle between them bisected by σ_1 and with their line of intersection parallel to σ_2. The size of the acute angle between the failure planes is related to the slope of the failure envelope (i.e., the friction coefficient—Table 1) [*Jaeger et al*., 2007]. Displacement occurs along a slip line contained within the failure plane and corresponding to the intersection of the failure plane with the plane containing σ_1 and σ_3 [*Anderson*, 1951].

[31] For tensile fracture, one failure plane forms and it is perpendicular to σ_3. Displacement occurs perpendicular to the failure plane (i.e., is opening mode [*Anderson*, 1951]).

[32] In reality, regardless of the sign of the normal stress, mixed-mode failure (shear and tensile) may occur as long as one of the principal stresses is tensile [*Twiss and Moores*, 1992]. In this case, two conjugate failure planes may form with an acute angle smaller than for shear failure and with components of both in-plane shear and opening. This consideration should be borne in mind when interpreting the model results shown below.

[33] To avoid running models to unrealistic elastic strains, the stresses were checked against the criterion at 5 MPa increments of reservoir pressure decrease. Elastic strains were considered unrealistic once either of two criteria was met. The first criterion is if fracturing affected a substantial subsurface part of the reservoir roof. In this case, the roof was considered to have exceeded its load-bearing capacity and undergone "ultimate failure." The second criterion is if regions considered to have failed in compression in a previous deflation increment subsequently went into tension. An example of the latter is shown in the supporting information (Figure S1).

[34] The actions of pore fluid pressures on the effective stresses and modes of failure are not included here, mainly because the incorporation of fluid-coupling in associated models is complex and well beyond the scope of this paper. Our models, nevertheless, represent a useful first step towards defining the general 3-D nature of faulting in roofs above magma chambers.

3.2. Analog Subsidence Models

3.2.1. Experimental Setup and Scaling

[35] The experimental setup comprised a sand/gypsum pack lying atop a table and enclosing a 2 cm-thick tabular (sill-like) reservoir of creamed honey (Figure 4). In most models, some dark grains of silicon carbide were added to the sand/gypsum surface to aid focusing of an overhead camera. A honey conduit ran from below the center of the reservoir to the base of the sand/gypsum pack, where it linked with a 0.8 cm diameter honey-filled pipe that ran through the table. Unplugging the pipe caused depletion of the reservoir and subsidence of the reservoir roof. For geometric scaling of the models, we chose a length ratio, $l^* = l_{\mathrm{Model}}/l_{\mathrm{Nature}}, = 1 \times 10^{5}$, such that 1 cm in the model scales to ~1 km in nature. The reservoir geometry was initially circular in plan view and 10 cm in diameter, and the reservoir depth was 2, 3, or 8 cm. For further construction

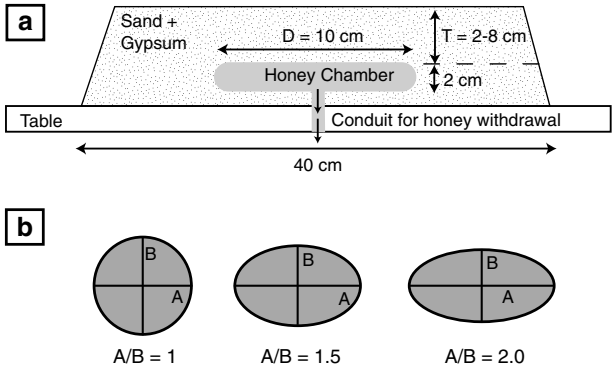

Figure 4. Setup of analog experiments. (a) Cross-sectional sketch of setup with circular reservoir; (b) map-view sketches of elliptical model reservoirs to show range of long axis/short axis (A/B) ratios investigated. For values of A and B for each ratio, see Table 2.

details, as well as discussion of dynamic and kinematic scaling, see *Holohan et al*. [2008a].

3.2.2. Particle Imaging Velocimetry

[36] The plan-view development of the model surface was recorded in time-lapse images taken at 60 s intervals by the overhead camera. Horizontal displacement vectors and strains were then calculated by means of a digital image correlation technique termed Particle Imaging Velocimetry (PIV) (Figure 5) in the commercially available software DaVis 7.2 by LaVision. With an 8 megapixel Canon EOS SLR, and a field of view of approximately 700×500 mm, the image resolution here is approximately 4 pixels mm^{-1}. Optical distortion was not corrected, but its influence should be minimal given the flat sand surface and the range of acquisition (approximately 1 m).

[37] To enhance the accuracy and spatial resolution of the displacement vector field, we used adaptive multipass correlation. This involved a first iteration with 32×32 pixel windows and 75% overlap, followed by two iterations with 12×12 pixel windows and 50% overlap. To increase the signal to noise ratio, displacement vectors were stacked with respect to every fifth image of the sequence. Default cutoff values were used to filter and disable spurious vectors. Any subsequent gaps in the vector field were filled by interpolation. These steps improved the displacement vector accuracy to <0.2 pixels or <0.05 mm (see also [*Adam et al*., 2005]).

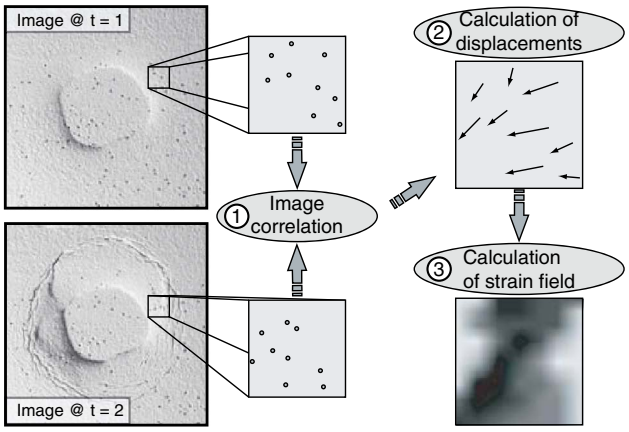

Figure 5. Outline of digital image correlation technique for calculation of displacement and strain fields. See main text for further explanation.

[38] The PIV results are shown in terms of cumulative horizontal displacements , as well as quantities derived from the components of the summed two-dimensional infinitesimal displacement gradient tensor. Dilatation

$$(dil = -E_{xx} - E_{yy}) \tag{4}$$

is a measure of the increase or decrease in horizontal area, which we interpret in terms of overall horizontal extension and contraction, respectively. Rotational strain component

$$(rotz = E_{yx} - E_{xy}) \tag{5}$$

is a measure of clockwise or anticlockwise rotation, which may occur synchronously with stretch (e.g., simple shear) or as a rigid body rotation. Where clearly spatially associated with a fault scarp, we interpret the rotational component in terms of simple shear and consider it to mark a sinistral or dextral strike-slip displacement component on the fault.

3.2.3. Cross-sections

[39] For final structural interpretations, we augmented the PIV by mapping fault scarp morphologies (normal dip-slip = sharp scarps; reverse dip-slip = blunt scarps). Once deformation had ceased, certain models were cross-sectioned by gently saturating the sand/gypsum pack with water, cutting it along orthogonal sections, and allowing it to harden.

3.3. Parameters Varied

[40] The thickness/diameter (T/D) ratio of the reservoir roof is the main parameter examined in our numerical and analog models because several previous studies showed that it strongly influences the mechanical and structural development of subsidence (e.g., [*Geyer et al*., 2006; *Roche et al*., 2000; *Zuber and Mouginis-Mark*, 1992]). For both the numerical models and the analog models, T/D ranges from 0.2 to 0.8. A subset of numerical analyses were made to check sensitivity to variations in model input properties such as Poisson's ratio, Young's modulus, as well as interpretation parameters, such as cohesion. A subset of analog models was made to examine three-dimensional effects from horizontal elongation of the reservoir (Figure 4b). T/D ratio varied azimuthally in such models, depending on the line of cross-section taken through the roof, but absolute reservoir depths were the same as for the circular cases. The parameters of the numerical and analog models shown below are summarized in Tables 1 and 2, respectively.

4. Numerical Modeling Results

4.1. Displacement Patterns

[41] Vertical or horizontal displacements show characteristic patterns in the numerical models. Vertical displacement increases with depth and with distance toward the reservoir center (Figure 6a). Horizontal displacement attains its highest values in a zone located near the surface and above the reservoir's lateral edges (Figure 6b). As shown below, this zone of high horizontal displacement coincides with regions of inferred oblique-slip faulting.

4.2. Regions and Modes of Failure

[42] The patterns of shear and tensile failure in the numerical models show many similarities for all T/D ratios

Table 2. List of Analog Models With Summary of Main Parameters and Structural Observations[a]

	Initial Parameters						Structural Observations						
Experiment	T (cm)	(A) (cm)	B (cm)	A/B	T/A	T/B	Sagging?	Wrinkle ridges?	Oblique-slip faults?	Off-centered subsidence?	Oblique-slip on ring fault?	Symmetry of strike-slip around caldera	Other Remarks
Cal Stat A3	2.0	9.9	9.7	1.0	0.2	0.2	Yes	Yes	O-R and O-N	Notably	No	Bilateral	No clear inner ring fault
Cal Stat C3	2.0	11.8	7.8	1.5	0.2	0.3	Yes	Yes	O-R and O-N	Notably	Slight, IRF	Bilateral	Quadrilateral symmetry initially
Cal Stat D3	2.0	12.9	6.8	1.9	0.2	0.3	Yes	Yes	O-R and O-N	Almost centered	No	Quadrilateral	
Cal Stat A2	3.0	10.5	10.2	1.0	0.3	0.3	Yes	Yes	O-R	Notably	IRF	Bilateral	
Cal Stat A5	3.0	10.4	10.3	1.0	0.3	0.3	Slight	No	O-R and O-N	Slightly	IRF	Radial/Bilateral	
Cal Stat C2	3.0	11.9	8.7	1.4	0.3	0.3	Slight	No	O-R and O-N	V. Notably	IRF and ORF	Bilateral	
Cal Stat C5	3.0	11.5	8.0	1.4	0.3	0.4	Slight	No	O-R and O-N	Slightly	IRF and ORF	Quad- / Bilateral	
Cal Stat D2	3.0	13.2	7.4	1.8	0.2	0.4	On long axis	Subtle	O-R	V. Slightly	No	Quadrilateral	Wrinkle ridges perpendicular to roof's long axis
Cal Stat D5	3.0	12.6	7.1	1.8	0.2	0.4	On long axis	Subtle	O-R and O-N	Slightly	IRF and ORF	Quad- / Bilateral	Wrinkle ridges perpendicular to roof's long axis
Cal Stat H1	8.0	10.0	10.0	1.0	0.8	0.8	V.V. slight	No	O-R	Slightly	Slight, IRF	Radial/Bilateral	
Cal Stat H2	8.0	10.0	10.0	1.0	0.8	0.8	V.V. slight	No	O-R	V. Slightly	Slight, IRF	Radial/Bilateral	
CalStat J1	8.0	13.5	6.4	2.1	0.6	1.3	V.V. slight	No	O-R and O-N	Slightly	IRF and ORF	Quadrilateral	
CalStat J2	8.0	13.2	6.6	2.0	0.6	1.2	V.V. slight	No	O-R	Almost centered	IRF	Quadrilateral	Reversal of central tilt and IRF strike-slip.
CalStat J3	8.0	13.1	6.7	2.0	0.6	1.2	V.V. slight	No	O-R	Notably	IRF	Bilateral	

[a] T = roof thickness, "A = roof long axis," and "B = roof short axis"; "O-R = oblique-reverse" and "O-N = oblique-normal"; IRF = inner ring fault and ORF = outer ring fault.

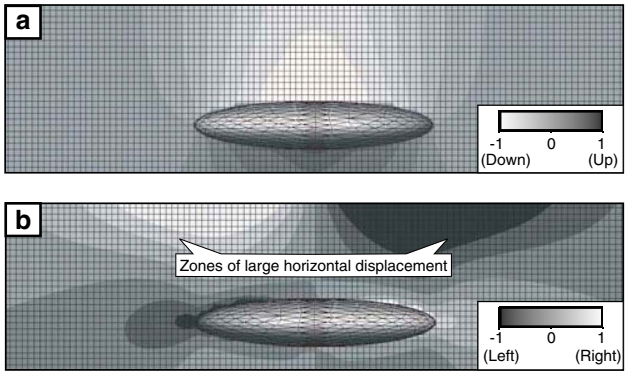

Figure 6. Displacement patterns in the BEM model for magma reservoir deflation. (a) Dimensionless vertical displacement. (b) Dimensionless horizontal displacement. The displacement patterns are as seen in any vertical plane of section passing through the reservoir center. They are purely illustrative and stem from an arbitrary pressure decrease in the reservoir. Also shown is the grid used for output of model stresses. The model here has $T/D = 0.4$, as in Figures 7b and 8.

(Figure 7). For brevity, the incremental development of failure in these models is not shown here, but an example is illustrated in the supporting information (Figure S1). The failure patterns and their evolution may be summarized as follows. Regions at the surface (depth = 0 km) fail first, with shear failure above the reservoir's center and with tensile or mixed-mode failure at a radial distance greater than the reservoir's diameter. Shallow subsurface regions (depth = 0–0.5 km) then fail at similar locations with further depressurization. At or below 0.5 km, failure in all locations tends to be exclusively in shear. Eventually, regions of shear failure form in the lower parts of the roof (depth >1 km). These are typically located at a radial distance equal to or slightly less than the reservoir diameter.

4.3. Orientations of Principal Stresses and Initial Fractures

[43] At ultimate failure, the stress fields resulting from gravity- and reservoir-induced loading also show many similarities for all T/D ratios (Figure 7). Principal stresses far away from the reservoir are horizontal or vertical in cross-section, while those closer to the reservoir are inclined. To mine or reservoir engineers, the inclination of principal stresses around a depleting subsurface body is known as "stress arching" [*Whittaker and Reddish*, 1989]. Stress arching in the models shown here is better developed in the reservoir roof than in the floor, and it becomes more pronounced with greater deflation (see Figure S1).

[44] We focus on four distinct three-dimensional stress states associated with regions of predicted shear failure in the reservoir roof (Figure 7). They are labeled (i)–(iv) in order of increased radial distance from the reservoir center. States (i) and (iii) are characterized by σ_2 and σ_3 lying within, and by σ_1 orientated normal to, the cross-sectional plane. They are restricted to the near-surface regions (depth <1 km) and spatially overlap the areas of high horizontal displacement (Figure 6). In contrast, states (ii) and (iv) are characterized by σ_1 and σ_3 lying within, and by σ_2 normal to, the cross-sectional plane.

[45] These stress states are associated with particular fault orientations and slip senses (Figures 8 and 9), depending on

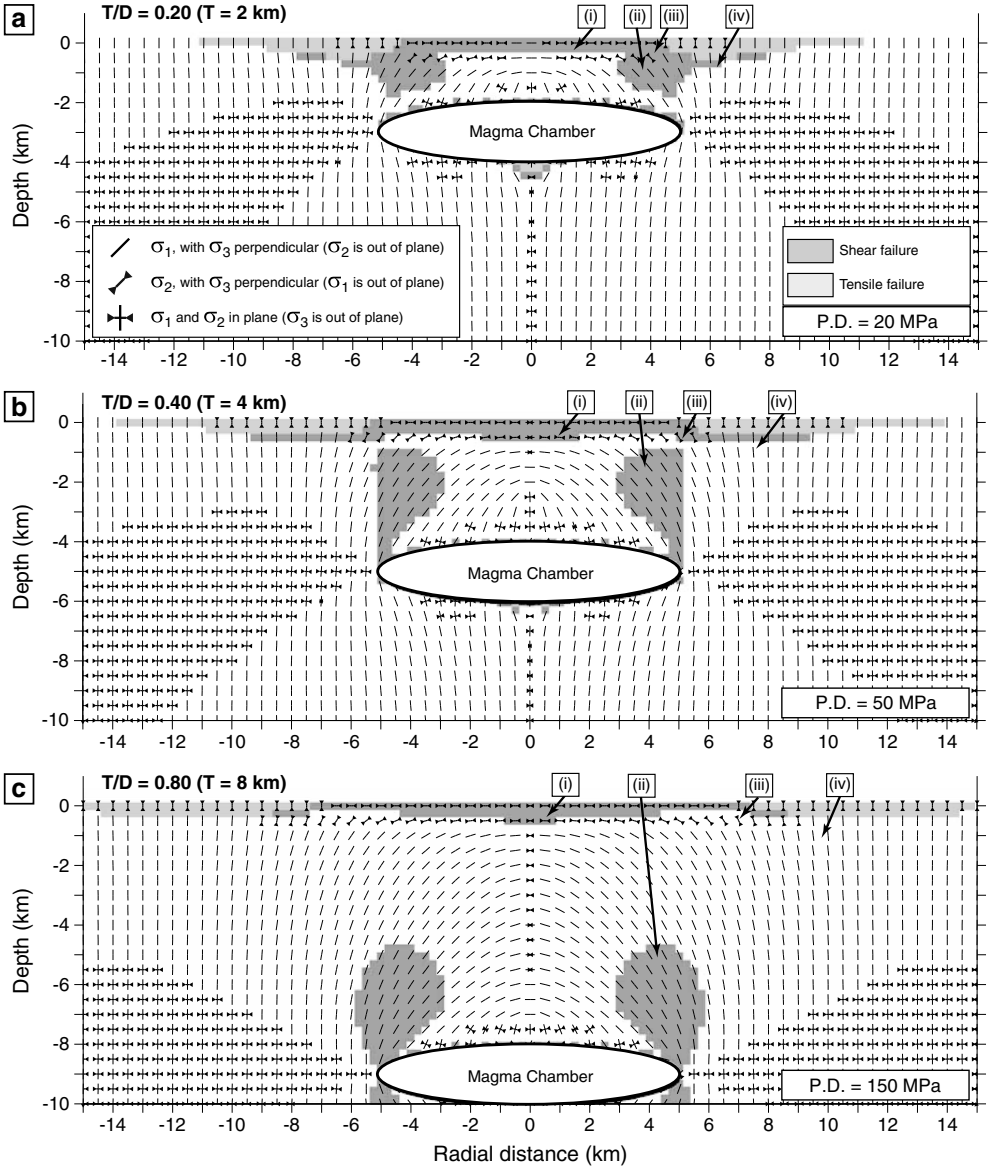

Figure 7. Principal stress orientations and potential failure zones resulting from superimposition of magma chamber deflation and gravitational stress fields. (a) $T/D = 0.2$; (b) $T/D = 0.4$; (c) $T/D = 0.8$. Results are shown along a radial plane of cross-section through each model and at the depressurization increment just after onset of major subsurface failure. The labels (i)–(iv) mark stress states compatible with structures formed in the analog models. P.D. = Pressure decrease applied to magma chamber wall.

the 3-D orientation of the principal stresses in each case [*Anderson*, 1951]. State (i) should produce reverse faults with radial strikes and shallow dips. State (ii) should result in faults with concentric strikes; one normal and with moderate outward dip, the other reverse and with steep outward dip. Regions affected by states (iii) and (iv) are predicted to fail simultaneously with or else after ultimate failure (Figure 7), so their positioning may not be so well constrained by the elastic modeling. State (iv) should result in normal faults with concentric strikes and moderate to steep dips. Importantly, state (iii) should produce oblique-reverse faults with strikes that are oblique to the concentric direction and with steep outward dips (Figures 8 and 9). Indeed, this analysis indicates that such oblique-reverse faults result wherever σ_1 is normal to, and σ_2 is inclined within, the plane of cross-section.

[46] Tensile or mixed-mode failure occurs at depths <0.5 km and at radial distances equal to or greater than the reservoir's radius (Figure 7). Mixed-mode fracture orientations and slip senses here may be similar to the shear failure predictions for states (iii) and (iv) (see above). Purely tensile failure along a single plane is probably only fully realized at the model surface, where confining pressure is near zero. Joints or fissures are likely to develop here [cf. *Schultz and Zuber*, 1994]; since σ_3 is horizontal, they should be vertical with concentric strike.

4.4. Effects of *T*/*D* Ratio

[47] Increasing *T*/*D* (i.e., depth) necessitates greater deflation to reach ultimate failure (Figure 7; see also *Geyer et al*. [2006]; *Roche and Druitt* [2001]). This is a result of the depth-dependent increase of confining pressure, a factor

that inhibits failure, as the "lithostatic" component of the gravitational stress field increases [*Twiss and Moores*, 1992].

[48] The distribution of failure regions also differs subtly as T/D ratio increases. Firstly, failure regions near the surface (depth = 0–0.5 km) occur at increased radial distances from the reservoir center (Figures 7a versus 7c). Secondly, the depth of fracturing is decreased in those near-surface failure regions. This suggests that initial fracturing will be less prominent there with increased roof thickness. Thirdly, the regions of failure at deeper levels in the roof are more clearly connected to the reservoir as T/D ratio increases. This suggests that failure along fractures in these regions may be enhanced with increased roof thickness.

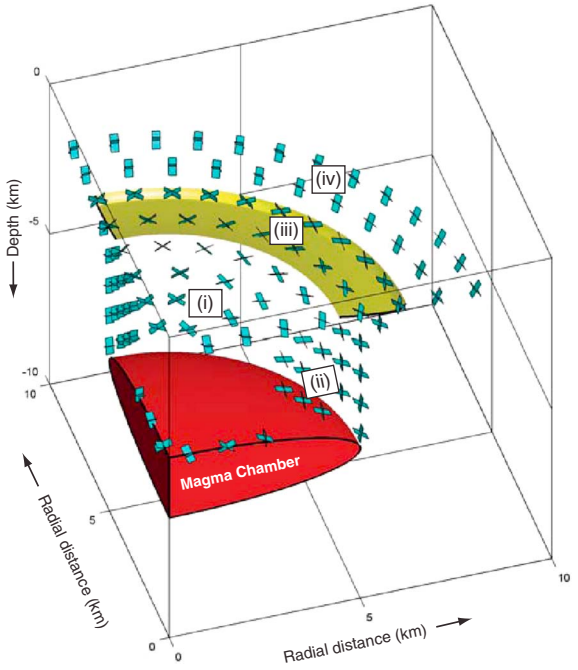

Figure 8. Orthographic projection of shear failure planes predicted from stress data in Figure 7b. For clarity, plotting is restricted to the cross-sections of the block and to a depth of 0.5 km for the plan-view face. The yellow surface marks the base of the zone where σ_2 lies in the radial plane and plunges steeply outward (>45°) from the roof center. Also marked are the areas of special interest (i)–(iv) in Figure 7, which link to the fault types shown in Figure 9.

4.5. Effects of Material Properties

[49] Increased Young's modulus decreases the magnitudes of strains and displacements attained for a particular deflation value. Otherwise, the main model results considered here, i.e., the patterns of displacements and stress orientations, as well as stress magnitudes at failure, failure location, and failure mode, are unaffected. Increased Poisson's ratio causes the following: (1) an increase in the pressure drop required to initiate fracturing; and (2) a reduction in the lateral extent of surface and near-surface fracturing beyond the reservoir radius. Material cohesion affects the onset and location of predicted fracturing in a similar manner to Poisson's ratio. This is because increasing Poisson's ratio moves a stress state away from the failure envelope by increasing the lithostatic mean stress whereas increasing cohesion moves the envelope away from a stress state by requiring greater differential stress to reach it.

5. Analog Modeling Results

[50] The temporal development of analog caldera subsidence and the structural effects of T/D and A/B ratios are well documented [e.g., *Burchardt and Walter*, 2010; *Holohan et al.*, 2008b; *Kennedy et al.*, 2004; *Marti et al.*, 1994; *Roche et al.*, 2000]. For brevity, we therefore detail

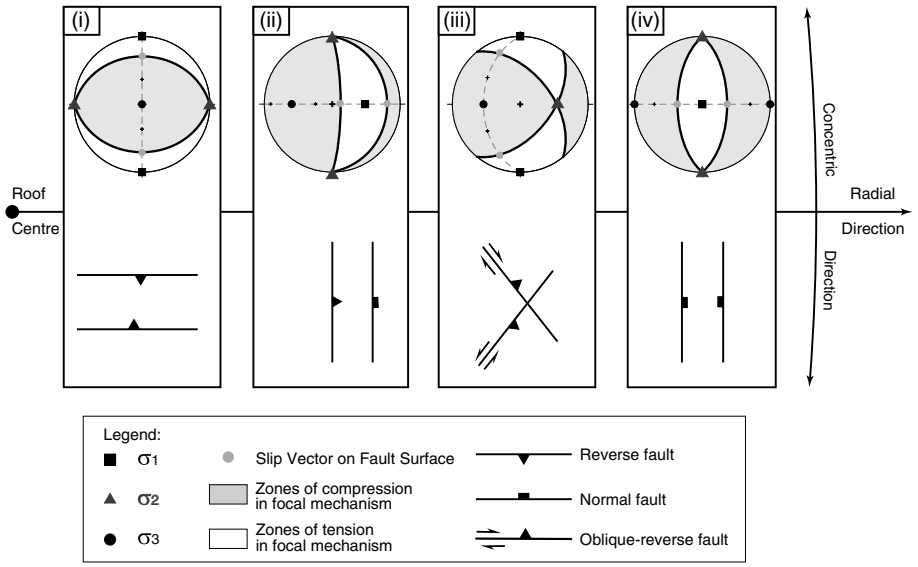

Figure 9. Predicted fault orientations and slip senses. Above are map-view stereonet projections (equal area, lower hemisphere) of the principal stress orientations and related shear failure planes at the points of special interest marked (i)–(iv) in Figures 7 and 8. Below are map-view traces of each failure plane. Note the oblique-slip faulting in state (iii).

our models' temporal evolutions in the supporting information (Figure S2). In general, these evolutions can be summarized as follows: (1) initial roof-wide sagging and marginal surface tensile fracturing; (2) central reverse (ring) faulting; and (3) peripheral normal (ring) faulting. T/D and A/B ratios strongly influence the details of this evolution, and below we recap those aspects relevant for contextualizing new observations of the following: (1) structural effects of off-centered subsidence; (2) horizontal displacement patterns; and (3) previously undocumented analog structures, such as wrinkle ridges and oblique-slip faults.

5.1. Central Zone Structures

[51] T/D ratio most strongly affects central zone structures. At $T/D < 0.3$, the model central zones undergo sagging (Figures 10a and 11a), which, relative to faulting, accommodates most of the reservoir roof's vertical displacement (Figure 12a).

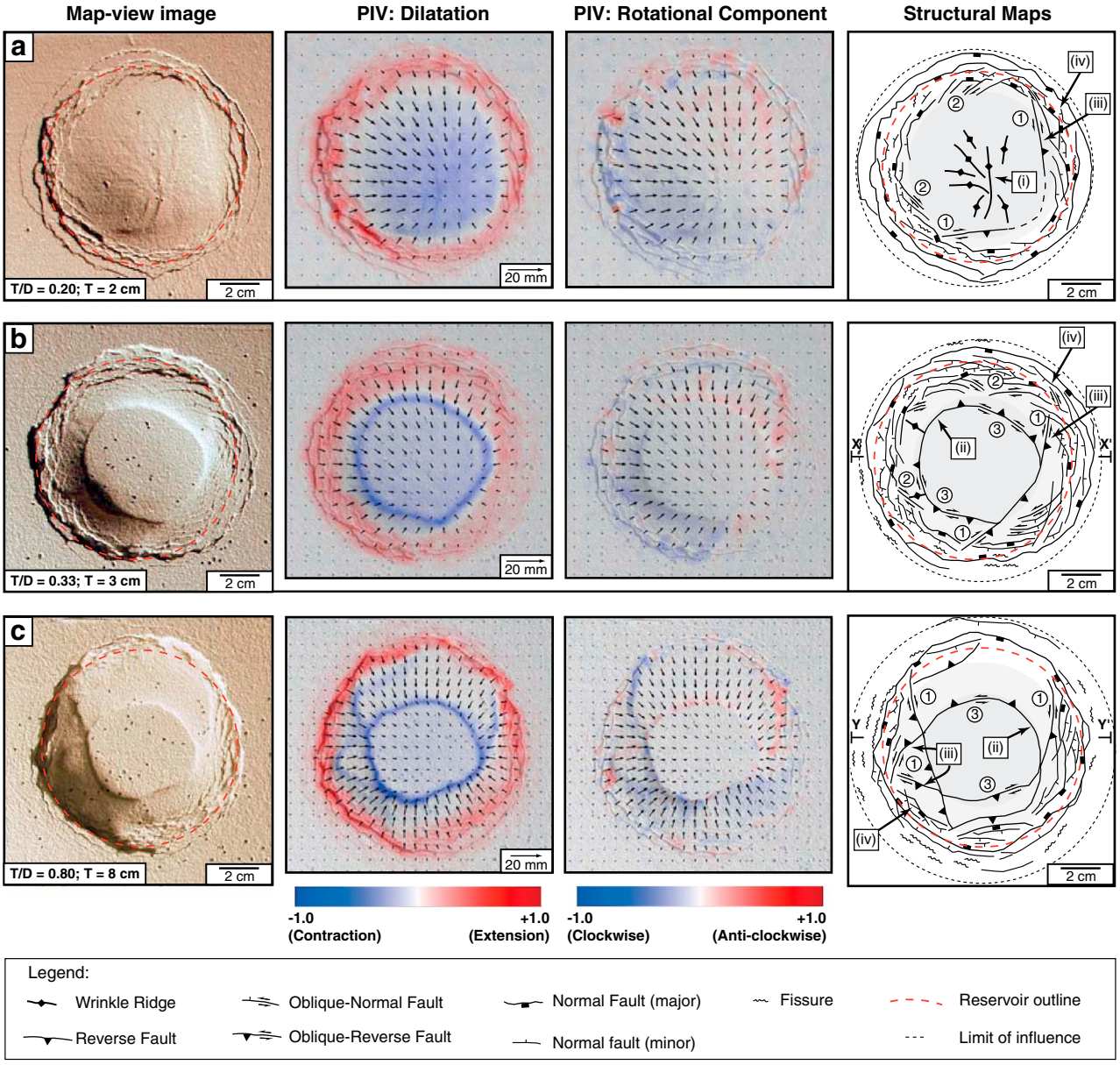

Figure 10. Results of analog caldera collapse into circular sill-like reservoirs. (a) $T = 2$ cm; (b) $T = 3$ cm; (c) $T = 8$ cm. Shown columnwise for each model are a final map-view image, the cumulative (i.e., finite) horizontal strains and displacements from PIV analysis, and a structural interpretation. For clarity, PIV images are taken at a slightly earlier stage of subsidence than in the final map-view image. The temporal evolution of each model is shown in Figure S2 in the supporting information. Color bar limits are absolute strain values (not normalized). Cross-sections along the lines marked X–X′ and Y–Y′ are shown in Figures 12b and 12c, respectively. Structures compatible with stresses shown in Figures 7, 8, and 9 are correspondingly marked (i), (ii), (iii), or (iv). Numbered circles refer to the four distinct settings of oblique-slip faulting described in the main text.

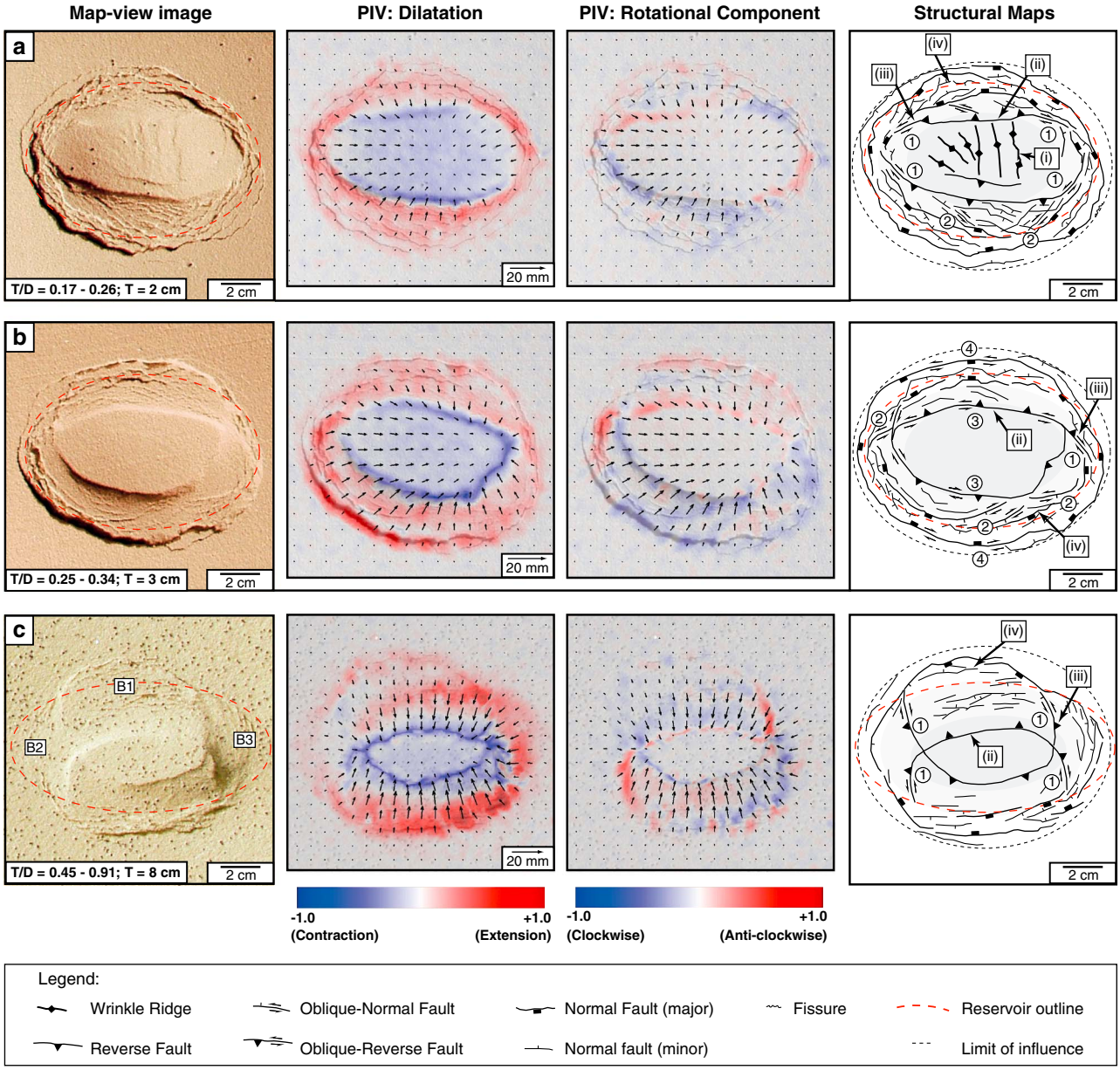

Figure 11. Results of analog caldera collapse into elliptical sill-like reservoirs. (a) $T/D = 0.17–0.26$, with $T = 2$ cm and $A/B = 1.4$; (b) $T/D = 0.25–0.34$, with $T = 3$ cm and $A/B = 1.5$; (c) $T/D = 0.45$-0.91, with $T = 8$ cm and $A/B = 2.0$. T/D ratio in elliptical reservoir roofs is variable, depending on the line of cross-section taken, and is hence given as a range between maximum and minimum values (along the roof's short and long axes, respectively). Fault-bound blocks in the periphery of the model in Figure 11c are labeled B1, B2, and B3 in order of development. See caption to Figure 10 for further explanation.

Radially trending wrinkle ridges form, which cross-sections show are near-surface structures. Arcuate reverse faults form along the sides of the central zone, but tend to be weakly developed. At $T/D > 0.3$, model central zones develop well-defined ring faults (Figures 10b, 10c, 11b, and 11c) that typically dip steeply outward with a large reverse slip component (Figure 12). At $T/D = 0.8$, sagging is negligible; ring faults accommodate most of the vertical displacement (e.g., Figure 12b and 12c).

[52] At low T/D, horizontal contraction increases steadily toward the roof center and reaches a maximum where the wrinkle ridges are best developed (Figures 10 and 11). With increased T/D, horizontal contraction is increasingly localized onto the central ring fault, and at $T/D = 0.8$, the enclosed central blocks show minimal horizontal strain.

5.2. Peripheral Zone Structures

[53] T/D ratio affects peripheral zone structures more subtly. Tensile fissures form with a near-concentric strike; they are generally vertical and occur just at the model surface. A network of marginal horsts and grabens and "step blocks" are defined by normal faults with concentric or near-concentric strike and steep inward or outward dip. A main

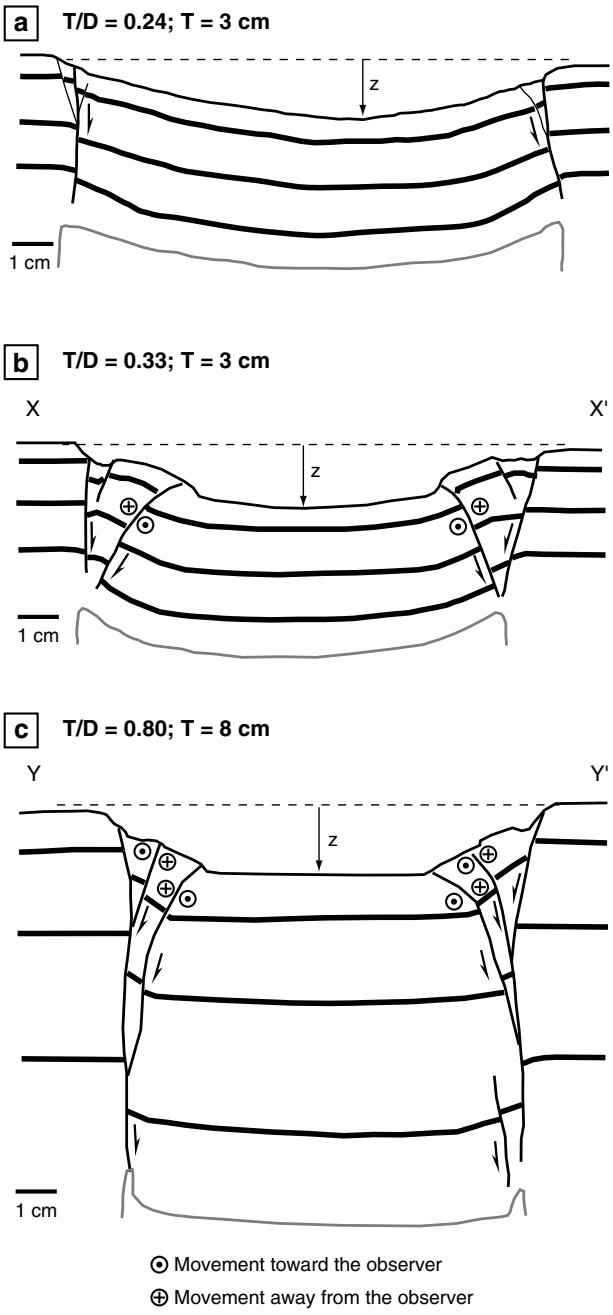

Figure 12. Line drawings of representative cross-sections though analog caldera models to show the effects of increased T/D on subsidence structures. (a) $T/D = 0.24$, (b) $T/D = 0.30$, (c) $T/D = 0.8$. The upper limit of the post-failure honey reservoir is marked by a gray line. The section in Figure 12a is taken from the elliptical model Cal Stat D5 (Table 2), but its T/D ratio and structure are representative of sections through the models in Figure 11a (long axis) and Figure 10a. The sections in Figures 12b and 12c are taken along the lines marked X–X′ in Figure 10b and Y–Y′ in Figure 10c, respectively. Increased T/D leads to a more rigid behavior of the roof, as the proportion of central vertical displacement, z, taken up by faulting increases, while the proportion taken up by sagging decreases.

outer ring fault also forms with inward dip and a large normal slip component (Figure 12). With increasing T/D, the peripheral zone diameter increases slightly (Figures 10 and 11), and horst and graben systems are generally more poorly developed (Figure 12b versus 12c).

5.3. Horizontal Displacements, Roof Elongation, and Off-Centered Subsidence

[54] Horizontal displacement vectors are generally directed in a radial manner toward an area of maximum subsidence within the central zone (Figures 10 and 11). At low T/D, in reflection of the distributed sagging, horizontal displacement magnitudes increase smoothly from the periphery, peak at a transitional area, and then decrease smoothly toward the center (e.g., Figure 10a). As T/D increases, horizontal displacements show an increasingly sharp discontinuity at the central ring fault trace. At $T/D = 0.8$, central zone and peripheral zone displacements are decoupled (e.g., Figures 10c and 11c).

[55] Roof elongation leads to the subtle effect of horizontal displacements being greatest along the roof's short axis (Figure 11). Associated structural effects are that ring faults [*Holohan et al.*, 2008b] and peripheral fault blocks (Figure 11c) tend to localize first along the short axis.

[56] The area of maximum subsidence is usually off-centered with respect to the reservoir outline, probably due to material heterogeneities [*Holohan et al.*, 2011; *Roche et al.*, 2000]. Rather than converging toward the caldera center, horizontal displacement vectors veer toward this off-centered area of maximum subsidence, and the roof as a whole undergoes a horizontal translation toward it. The translation magnitude is smallest in relatively centered subsidence (e.g., Figures 10c and 11a) and largest in highly off-centered subsidence (e.g., Figure 11b). The translation is most strongly expressed in the central zone and more subtly so in the peripheral zone, a contrast accentuated by structural decoupling of these zones via ring faults at higher T/D.

[57] The main structural effect of off-centered subsidence is to accentuate horizontal contraction at the side of the roof toward which the bulk translation is directed. Reverse faulting is consequently better developed at this side, whether as arcuate faults (e.g., Figure 10a) or as ring faults (e.g., Figure 11b). Horizontal extension is conversely accentuated on the opposite side of the roof, and so normal faulting is typically better developed here. Such an opposite development of normal and reverse faulting with off-centered subsidence is subtly expressed in the upper levels of the cross-section in Figure 12a.

5.4. Oblique-Slip Faulting

[58] In the plan-view PIV images, faulting with a strike-slip component is manifested by localized contours of the rotational component of strain. Decorrelation arising mainly from complex fracturing and scarp collapse can produce noise in the rotational strain signal. This is particularly prevalent in the peripheral zone, and so interpretations there require greater care. The signal is well resolved overall, however, and reveals strike-slip component faulting in four settings. Settings (1) and (2) typically occur in the transition between the zones of peripheral extension and central contraction. They develop after substantial sagging or after localization of the central ring fault (see Figure S2).

Settings (3) and (4) occur on ring faults and are associated with off-centered subsidence.

[59] Setting (1) is oblique-reverse slip on a fault segment trending obliquely to the reservoir outline. This occurs either at the lateral end of an arcuate reverse fault or as a splay from a central ring fault. Some neighboring oblique-reverse faults show an apparent conjugate relationship (differently trending traces with opposite shear senses) (e.g., Figures 10c and 11c). Cross-sections through some oblique-reverse splays (Figure 10c) reveal that they dip steeply outward and are located at relatively shallow levels in the roof (Figure 12c).

[60] Setting (2) is oblique-normal slip along an obliquely trending fault segment. This commonly occurs within the peripheral zone as a splay from a concentric normal fault, either a major graben bounding fault or the outer ring fault. Again, some neighboring oblique-normal faults show apparent conjugate relationships (e.g., Figure 11b).

[61] Settings (1) and (2) are slightly influenced by roof elongation and off-centered subsidence. With an elongated roof, the oblique-reverse faults tend to form towards the ends of the roof's long axis (e.g., Figures 11a and 11c). With off-centered subsidence, oblique-reverse faults tend to form on the side toward which the horizontal translation occurs, whereas oblique-normal faults tend to form on the opposite side (Figures 10a, 10b, and 11c).

[62] Setting (3) is oblique-reverse slip on a central ring fault. Setting (4) is oblique-normal slip on an outer ring fault. During subsidence that is only slightly off-centered, oblique slip is subtle and detectable only on the inner ring fault (e.g., Figure 10c). When off-centeredness of subsidence is significant, oblique-slip is detectable on both inner and outer ring faults (e.g., Figure 11b).

6. Discussion

6.1. Comparison of Numerical and Analog Results

[63] A feature of past caldera subsidence studies has been the dissimilarity of many results (or interpretations) from analog and continuum-based numerical approaches (e.g., *Gudmundsson et al*. [1997] versus *Roche et al*. [2000]). While differences also arose between the results of both approaches in our study, they are minor compared to some previous studies. Rather, the overriding similarity of each approach's results shows their complementary natures when conducted with robust scaling relationships and appropriate failure criteria [*Sanford*, 1959].

6.1.1. Similarities

[64] In terms of location, the numerical and analog results both include the following structures:

[65] (1) Thrusts with radial strike (wrinkle ridges), located near the surface and above the reservoir center (state (i) in Figures 7–9).

[66] (2) Reverse faults with concentric strike and steep outward dip, located at deeper levels and above the reservoir's lateral margins (state (ii) in Figures 7–9).

[67] (3) Vertical tensile fractures with concentric strike or peripheral normal faults with concentric strike, and inward or outward dips, located near surface and beyond the reservoir's lateral margins (state (iv) in Figures 7–9).

[68] (4) Oblique-reverse faults with an oblique strike and a steep outward dip that are located near the surface and roughly above or just within the reservoir's lateral margins (state (iii) in Figures 7–9).

[69] In terms of the timing of faulting, both approaches produce the following sequence:

[70] (1) Tensile fracturing at surface beyond the reservoir margins.

[71] (2) Formation of steeply outward-inclined reverse faults.

[72] (3) Late-phase formation of oblique-reverse faults and of normal ring faults.

[73] This striking agreement indicates that our numerical approach can provide reliable mechanical insights into the observed incidences of oblique-slip faulting in the analog models and in nature.

6.1.2. Differences

[74] The numerical prediction of near-surface radial thrusts (i.e., wrinkle ridges) at $T/D > 0.3$ (Figure 7) is not observed in the experiments. At $T/D = 0.8$, the numerical results predict that stress states (iii) and (iv) occur well outside the reservoir's lateral margin (Figure 7), which is not in agreement with where oblique-reverse and normal faults form in comparable analog models (e.g., Figure 12). These disparities probably reflect the differences or limitations in the modeling approaches, such as the scaling of elastic properties and the continuum-based method's diminished predictive capacity beyond the initial stages of fracturing.

[75] Finally, the oblique-normal faults observed in the experiments are not predicted from the numerical analysis. One explanation, consistent with Andersonian faulting, is that oblique-normal faults stem from local rotation of all three principal stresses out of the radial plane during the later stages of subsidence, as the growth and interaction of discontinuities create local deviations from the general stress pattern. Alternatively, the oblique-normal faults may be predicted from 3-D strain theory [e.g., *Krantz*, 1988] compatible with stress state (iv), but full exploration of this hypothesis is beyond the scope of the present paper.

6.2. Mechanical and Kinematic Explanations for Oblique-Slip Faulting at Calderas

6.2.1. The "Camera Iris" Effect

[76] Subsidence involves not only vertical displacement but also horizontal movement. This is recorded at calderas [e.g., *Michon et al*., 2009] (Figure 1c), mines [e.g., *Whittaker and Reddish*, 1989], and hydrocarbon reservoirs [e.g., *Yerkes and Castle*, 1976]. Horizontal movements are directed toward the center of the subsiding area and lead to zones of inner radial shortening and outer radial extension [*Branney*, 1995; *Whittaker and Reddish*, 1989]. As explained below, inward horizontal displacement can also lead to strike-slip component faulting (Figure 13a).

[77] For most of the roof, displacement is dominantly vertical or near-vertical toward the deflating reservoir (Figure 6a). In combination with lithostatic stress, this means that σ_1 typically lies in the vertical plane of cross-section and wraps around the reservoir to form a "stress arch" (Figure 7). In some parts of the roof, however, horizontal displacement is also significant (Figure 6b). This inward radial movement generates a concentric shortening and a related compressive "hoop stress" in the horizontal plane (Figure 13a). If the horizontal displacement gradient is high enough, the hoop stress may be σ_1, in which case σ_2 switches into the stress arch

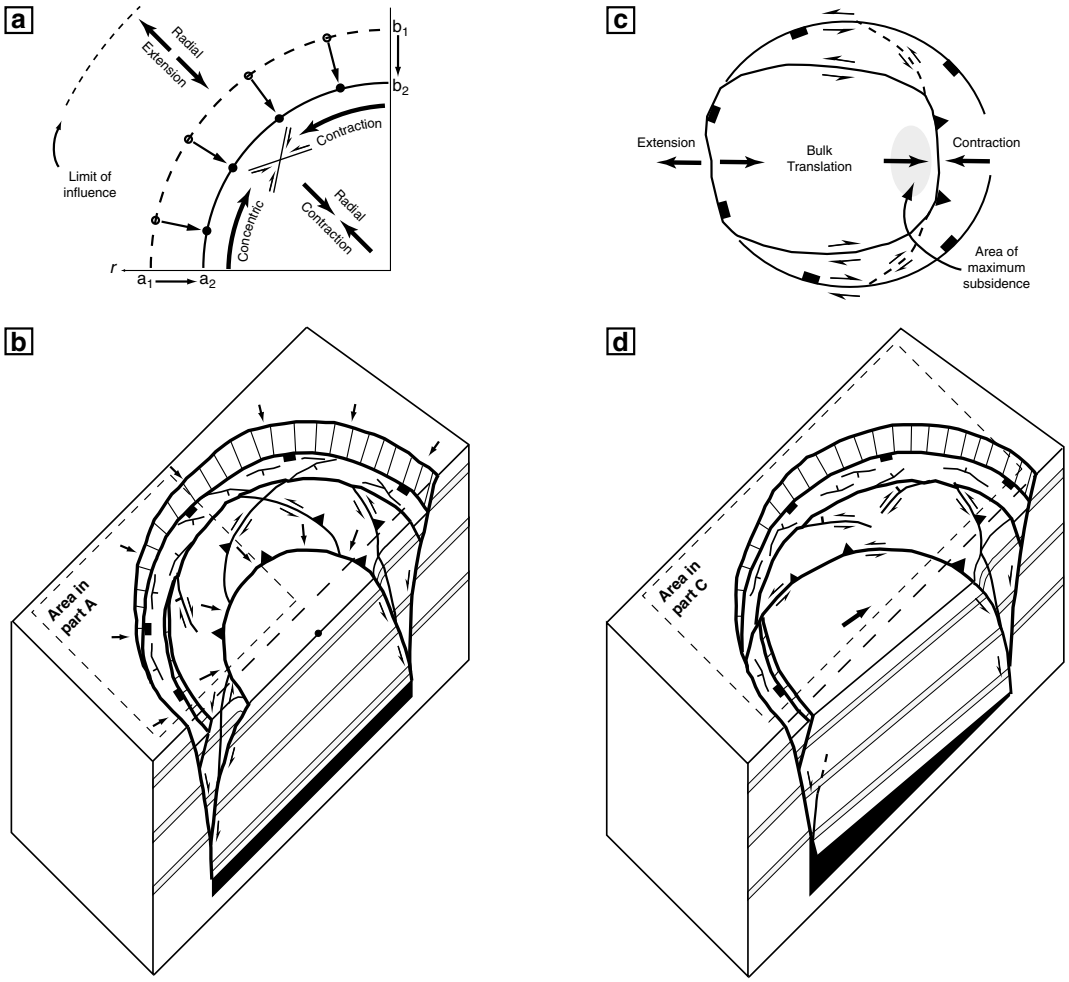

Figure 13. Summary of the two origins of oblique-slip faulting identified in this study. (a) Illustration of how circumferential horizontal shortening results as material points move radially inward (note reduction of arc length from a1–b1 to a2–b2). This is accommodated by the strike-slip components of fault displacements, producing the camera iris effect; (b) block diagram of centered subsidence with oblique-slip faults related to the camera iris effect. The area of the roof delimited by dashed box is roughly that considered in Figure 13a; (c) Illustration of how strike-slip component faulting stems from horizontal translation of the down-going roof during off-centered subsidence. (d) Block diagram of off-centered subsidence with oblique-slip faults related to the sliding trapdoor effect.

in the radial plane. According to Anderson's theory, this mechanical condition (state (iii) in Figures 7–9) produces oblique-slip faults.

[78] Kinematically, a strike-slip displacement component on an obliquely trending fault accommodates this concentric shortening and hence relaxes the compressive hoop stress (Figure 13a). A dip-slip component on such a fault then accommodates either shortening (oblique-reverse) or extension (oblique-normal) in the radial direction. Oblique-slip faults hence enable sections of the caldera periphery to move horizontally inward by sliding past and/or over each other, in a manner that is analogous to the closure of a camera "iris" (Figure 13b).

6.2.2. The "Sliding Trapdoor" Effect

[79] Off-centered subsidence ("trapdoor" or "asymmetric") is a common feature of natural calderas [*Lipman*, 1997]. In the analog models, it is linked with a horizontal translation toward the area of maximum subsidence. Consequently, reverse ring faults preferentially develop on the side of the caldera toward which the horizontal translation is directed, and normal ring faults preferentially develop on the side opposite (Figure 13c). Displacement on the ring faults at these locations will be purely dip-slip. However, slip elsewhere around the ring faults must include a strike-slip component that accommodates the horizontal translation of the roof mass enclosed by the ring fault (Figure 13c). Kinematically, this system of reverse, strike-slip, and normal faulting is analogous to a sliding trapdoor (Figure 13d).

6.2.3. Superposition of Both Effects

[80] The "camera iris" effect is most clearly seen with centered or near-centered subsidence. The orientations and shear senses of oblique-slip faults approach a radial symmetry in the circular roof (e.g., Figures 7 and 10c) and a quadrilateral symmetry in the elongate roof (e.g., Figure 8c).

The horizontal translation associated with off-centered subsidence imparts a bilateral symmetry in shear sense (e.g., Figures 7a and 8b). This overprints but does not entirely overwhelm the "iris-like" effect, which is seen as neighboring oblique-normal or oblique-reverse faults of opposite (synthetic) shear sense even with highly off-centered subsidence (e.g., Figures 7b and 8b). This illustrates how the contributions of both mechanisms can be recognized when acting together, as is likely in nature.

[81] Far-field or regional tectonic stresses may additionally superimpose on gravity and reservoir stresses in nature. Such stresses will impart further 3-D variation into the total stress field and hence influence the location of oblique-slip faulting and related seismicity. An analog and analytical study by *Withjack and Scheiner* [1982] shows such influences on strike-slip component faults formed during doming, and we anticipate that these results can be extrapolated to the case of subsidence.

6.3. Comparison to Natural Calderas

6.3.1. Olympus Mons

[82] Structural relationships in Olympus Mons caldera are remarkably similar to those in circular-roof models with $T/D = 0.2$ (compare Figures, 1a, 7a, and 10a). In nature and models, oblique-slip faults occur in a transitional area between central contraction (sagging plus wrinkle ridges) and peripheral extension (normal faults). The model results therefore support our reinterpretation of the enigmatic "concentric ridges" as oblique-slip faults and indicate that in addition to concentric shortening they may accommodate either radial contraction [*Zuber and Mouginis-Mark*, 1992] or radial extension (i.e., the inferred dip-slip component could be normal or reverse).

[83] Radially striking thrusts or folds, as in the radial "wrinkle ridges" in the center of Olympus Mons caldera [*Plescia and Golombek*, 1986] also accommodate concentric horizontal shortening. Our models show that "wrinkle ridge" formation is linked with sagging and promoted by a low T/D ratio, a geometric attribute previously inferred independently for Olympus Mons caldera [*Zuber and Mouginis-Mark*, 1992].

6.3.2. Miyakejima

[84] There are several structural similarities between Miyakejima caldera and the elliptical-roof models with $T/D = 0.8$ (compare Figures 1b and 11c). Firstly, formation of the outer normal ring fault involves inward sliding of several marginal blocks, initially along the caldera's short axis and then at the long axis. Oblique-slip faults accommodate the initial inward block motions. In the models, these faults are mainly oblique-reverse but sometimes oblique-normal. In both model and nature, the oblique-slip faults again occur in a transitional area between central contraction and peripheral extension.

[85] Secondly, the off-centered position of maximum subsidence at the northeast end of Miyakejima caldera seems to have entailed horizontal displacement of the central block to the northeast (Figure 1b). If so, the analog model results (e.g., Figure 11b) support an interpretation of oblique-slip on Miyakejima caldera's inner ring fault.

[86] Thirdly, the oblique-slip faults at Miyakejima (Figure 1b) and in the models (e.g., Figures 11a and 11c) localized near the ends of caldera's long axis. This is consistent with numerical models of mining subsidence [*Whittaker and Reddish*, 1989], which show a maximum horizontal circumferential stress at the long-axis ends of the mine's roof. One explanation is that oblique-slip faults here accommodate a horizontal shear caused by the greater inward horizontal displacement along the short axis. Another is that circumferential shortening is greater near the end of the long axis because the roof's plan-view curvature is highest here.

6.3.3. Dolomieu

[87] Although we limited our models to $T/D < 1$, their results allow us to make some inferences about how oblique-slip faulting may manifest at depth in cases where $T/D > 1$, such as at Dolomieu caldera ($T/D \sim 2.0$) [*Michon et al*., 2009]. Our $T/D = 0.8$ models show that oblique-slip faults localize between the reverse and normal ring faults as a result of displacement along either or both of these structures (e.g., Figures 10c and 11c). Past modeling studies [e.g., *Holohan et al*., 2011; *Roche et al*., 2000] show that $T/D > 1$ leads to a vertical succession of such normal and reverse ring faults. Hence, oblique-slip faults are inferred to form not only near the surface but also at depth, wherever sufficient horizontal inward displacement occurs along inward- or outward-dipping ring faults. This inference may help explain the abundance of oblique-slip earthquake source mechanisms observed at depth during the 2007 Dolomieu collapse [*Massin et al*., 2011] (Figure 1c).

6.4. Implications for Nondouble Couple Focal Mechanisms at Calderas and Mines

[88] Subsidence at calderas and mines often generates nondouble couple earthquakes with an unusually large compensated linear vector dipole (CLVD) component. Some finite source inversion studies link CLVD-dominated earthquakes with slip along outward- or inward- dipping ring faults [e.g., *Ekstrom*, 1994]. Other studies explain them as a combination of simultaneous strike-slip and dip-slip on separate planar faults [*Miller et al*., 1998].

[89] Our models highlight possibilities for a dip-slip plus strike-slip combination not only on separate faults but also on a single ring fault. For off-centered subsidence, experimental ring faults are often inward-inclined on one side and outward-inclined on the other (Figure 12a), as is seen in nature at the "asymmetrically subsided" Glencoe caldera, Scotland [*Clough et al*., 1909; *Kokelaar and Moore*, 2006]. Such a ring-fault geometry is inferred for a major collapse event at Bardarbunga caldera, Iceland, on the basis of an associated CLVD earthquake focal mechanism [*Fichtner and Tkalcic*, 2010]. As in other ring fault based CLVD source mechanism studies to date, however, displacements were assumed to be purely dip-slip. Our models show that such ring fault geometries necessitate a strike-slip component also, which should hence be included in future CLVD source mechanism studies.

7. Conclusions

[90] A joint analysis of numerical and analog subsidence models yields evidence for two distinct origins of oblique-slip faulting during caldera collapse in nature.

[91] The first origin, termed the "camera iris" mechanism, occurs as a response to horizontal displacements of the

reservoir roof that are directed radially inward. These arise either from centroclinal bending (down-sagging) or from slip along inclined ring faults. The radial horizontal displacements induce a concentrically orientated shortening (and associated compression) that is accommodated by a strike-slip component of displacement on oblique-reverse or oblique-normal faults that strike obliquely to the caldera center.

[92] The second origin, termed the "sliding trapdoor" mechanism, occurs as a response to horizontal translation of the reservoir roof arising from off-centered (or "asymmetric") subsidence. This horizontal translation is mainly accommodated by oblique-reverse or oblique-normal slip on arcuate faults and, in particular, on ring faults.

[93] As in nature, model strike-slip component faults typically occur at a transition between an inner zone of dominantly reverse faulting and an outer zone of dominantly normal faulting.

[94] These results provide a more complete three-dimensional understanding of structures and earthquakes related to caldera subsidence. Consequently, they may better contextualize structural and geophysical observations during subsidence above mines or hydrocarbon reservoirs.

[95] **Acknowledgments.** M. Shirzaei and H. Sudhaus helped with visualization of the numerical results. M. Rosenau assisted with DaVis, and A. Shuler stimulated our interest in CLVD events. N. Geshi and H. Murakami kindly provided images and discussion of the 2000 Miyakejima collapse event. E.P.H. acknowledges an INSPIRE international-mobility fellowship cofunded by Marie Curie Actions and the Irish Research Council.

References

Adam, J., J. L. Urai, B. Wieneke, O. Oncken, K. Pfeiffer, N. Kukowski, J. Lohrmann, S. Hoth, W. van der Zee, and J. Schmatz (2005), Shear localisation and strain distribution during tectonic faulting—New insights from granular-flow experiments and high-resolution optical image correlation techniques, *J. Struct. Geol.*, *27*(2), 283–301.

Anderson, E. M. (1936), The dynamics of the formation of cone-sheets, ring-dykes, and cauldron subsidences, *Proc. Royal Soc. Edinburgh*, *56*, 128–157.

Anderson, E. M. (1951), *The Dynamics of Faulting and Dyke Formation With Applications to Britain*, 2nd ed., Oliver & Boyd, Edinburgh, Scotland.

Branney, M. J. (1995), Downsag and extension at calderas—New perspectives on collapse geometries from ice-melt, mining, and volcanic subsidence, *B. Volcanol.*, *57*(5), 303–318.

Burchardt, S., and T. R. Walter (2010), Propagation, linkage, and interaction of caldera ring-faults: Comparison between analogue experiments and caldera collapse at Miyakejima, Japan, in 2000, *B. Volcanol.*, *72*(3), 297–308.

Clough, C. T., H. B. Maufe, and E. B. Bailey (1909), The cauldron-subsidence of Glencoe and associated igneous phenomena, *J. Geol. Soc. London*, *64*, 611–676.

Crumpler, L. S., J. W. Head, and J. C. Aubele (1996), Calderas on Mars; characteristics, structure, and associated flank deformation, in *Volcano Instability on the Earth and Other Planets*, edited by W. J. McGuire, A. P. Jones and J. Neuberg, pp. 307–348, Geological Society of London, London, U.K.

Ekstrom, G. (1994), Anomalous earthquakes on volcano ring-fault structures, *Earth Planet Sc. Lett.*, *128*(3–4), 707–712.

Fichtner, A., and H. Tkalcic (2010), Insights into the kinematics of a volcanic caldera drop: Probabilistic finite-source inversion of the 1996 Bardarbunga, Iceland, earthquake, *Earth Planet Sc. Lett.*, *297*(3–4), 607–615.

Geshi, N., T. Shimano, T. Chiba, and S. Nakada (2002), Caldera collapse during the 2000 eruption of Miyakejima Volcano, Japan, *B. Volcanol.*, *64*(1), 55–68.

Geyer, A., and J. Marti (2008), The new worldwide collapse caldera database (CCDB): A tool for studying and understanding caldera processes, *J. Volcanol. Geoth. Res.*, *175*(3), 334–354.

Geyer, A., A. Folch, and J. Marti (2006), Relationship between caldera collapse and magma chamber withdrawal: An experimental approach, *J. Volcanol. Geoth. Res.*, *157*(4), 375–386.

Gudmundsson, A., J. Marti, and E. Turon (1997), Stress fields generating ring faults in volcanoes, *Geophys. Res. Lett.*, *24*(13), 1559–1562.

Holohan, E. P., B. van Wyk de Vries, and V. R. Troll (2008a), Analogue models of caldera collapse in strike-slip tectonic regimes, *B. Volcanol.*, *70*(7), 773–796.

Holohan, E. P., V. R. Troll, B. van Wyk de Vries, J. J. Walsh, and T. R. Walter (2008b), Unzipping Long Valley: An explanation for vent migration patterns during an elliptical ring fracture eruption, *Geology*, *36*(4), 323–326.

Holohan, E. P., M. P. J. Schöpfer, and J. J. Walsh (2011), Mechanical and geometric controls on the structural evolution of pit crater and caldera subsidence, *J. Geophys. Res.*, *116*.

Jaeger, J. C., N. G. W. Cook, and R. W. Zimmerman (2007), *Fundamentals of Rock Mechanics*, 4th ed. ed., Blackwell, Malden, Mass., Oxford, U.K.

Jeyakumaran, M., J. W. Rudnicki, and L. M. Keer (1992), Modeling slip zones with triangular dislocation elements, *B. Seismol. Soc. Am.*, *82*(5), 2153–2169.

Kennedy, B., J. Stix, J. W. Vallance, Y. Lavallee, and M. A. Longpre (2004), Controls on caldera structure: Results from analogue sandbox modeling, *Geol. Soc. Am. Bull.*, *116*(5-6), 515–524.

Kokelaar, B. P., and I. D. Moore (2006), Glencoe caldera volcano, Scotland, British Geological Survey, Nottingham.

Krantz, R. W. (1988), Multiple fault sets and 3-dimensional strain—theory and application, *J. Struct. Geol.*, *10*(3), 225-&.

Latter, J. (1981), Tsunamis of volcanic origin: Summary of causes, with particular reference to Krakatoa, 1883, *B. Volcanol.*, *44*(3), 467–490.

Lipman, P. W. (1997), Subsidence of ash-flow calderas: Relation to caldera size and magma-chamber geometry, *B. Volcanol.*, *59*(3), 198–218.

Marti, J., G. J. Ablay, L. T. Redshaw, and R. S. J. Sparks (1994), Experimental studies of collapse calderas, *J. Geol. Soc. London*, *151*, 919–929.

Massin, F., V. Ferrazzini, P. Bachelery, A. Nercessian, Z. Duputel, and T. Staudacher (2011), Structures and evolution of the plumbing system of Piton de la Fournaise volcano inferred from clustering of 2007 eruptive cycle seismicity, *J. Volcanol. Geoth. Res.*, *202*(1–2), 96–106.

Michon, L., N. Villeneuve, T. Catry, and O. Merle (2009), How summit calderas collapse on basaltic volcanoes: New insights from the April 2007 caldera collapse of Piton de la Fournaise volcano, *J. Volcanol. Geoth. Res.*, *184*(1–2), 138–151.

Miller, A. D., G. R. Foulger, and B. R. Julian (1998), Non-double-couple earthquakes 2. Observations, *Rev. Geophys.*, *36*(4), 551–568.

Moore, I., and P. Kokelaar (1998), Tectonically controlled piecemeal caldera collapse: A case study of Glencoe volcano, Scotland, *Geol. Soc. Am. Bull.*, *110*(11), 1448–1466.

Mori, J., and C. Mckee (1987), Outward-dipping ring-fault structure at Rabaul Caldera as shown by earthquake locations, *Science*, *235*(4785), 193–195.

Mouginis-Mark, P. J., and M. S. Robinson (1992), Evolution of the Olympus Mons Caldera, Mars, *B. Volcanol.*, *54*(5), 347–360.

Odonne, F., I. Menard, G. J. Massonnat, and J. P. Rolando (1999), Abnormal reverse faulting above a depleting reservoir, *Geology*, *27*(2), 111–114.

Paul, B. (1961), A modification of the Coulomb-Mohr theory of fracture, *J. App. Mech.*, *28*(2).

Plescia, J. B., and M. P. Golombek (1986), Origin of planetary wrinkle ridges based on the study of terrestrial analogs, *Geol. Soc. Am. Bull.*, *97* (11), 1289–1299.

Roche, O., and T. H. Druitt (2001), Onset of caldera collapse during ignimbrite eruptions, *Earth Planet Sc. Lett.*, *191*(3–4), 191–202.

Roche, O., T. H. Druitt, and O. Merle (2000), Experimental study of caldera formation, *J. Geophys. Res.-Sol. Ea.*, *105*(B1), 395–416.

Rytuba, J. J. (1994), Evolution of volcanic and tectonic features in caldera settings and their importance in the localization of ore-deposits, *Econ. Geol. Bull. Soc.*, *89*(8), 1687–1696.

Sanford, A. R. (1959), Analytical and experimental study of simple geologic structures, *Geol. Soc. Am. Bull.*, *70*(1), 19-&.

Schultz, R. A., and M. T. Zuber (1994), Observations, models, and mechanisms of failure of surface rocks surrounding planetary surface loads, *J. Geophys. Res.-Planet*, *99*(E7), 14,691–14,702.

Staudacher, T., V. Ferrazzini, A. Peltier, P. Kowalski, P. Boissier, P. Catherine, F. Lauret, and F. Massin (2009), The April 2007 eruption and the Dolomieu crater collapse, two major events at Piton de la Fournaise (La Reunion Island, Indian Ocean), *J. Volcanol. Geoth. Res.*, *184*(1–2), 126–137.

Stix, J., and T. Kobayashi (2008), Magma dynamics and collapse mechanisms during four historic caldera-forming events, *J. Geophys. Res.-Sol. Ea.*, *113*(B9).

Thomas, A. L. (1993), Poly3D: A three-dimensional, polygonal element, displacement discontinuity boundary element computer program with applications to fractures, faults, and cavities in the Earth's crust, Masters thesis, 69 pp., Stanford University.

Toda, S., R. S. Stein, and T. Sagiya (2002), Evidence from the AD 2000 Izu islands earthquake swarm that stressing rate governs seismicity, *Nature*, *419*(6902), 58–61.

Twiss, R. J., and E. M. Moores (1992), *Structural Geology*, xii, 532 p. pp., W.H. Freeman, New York.

Walker, G. P. L. (1984), Downsag calderas, ring faults, caldera sizes, and incremental caldera growth, *J. Geophys. Res.*, *89*(Nb10), 8407–8416.

Walter, T. R., and V. R. Troll (2001), Formation of caldera periphery faults: An experimental study, *B. Volcanol.*, *63*(2–3), 191–203.

Whittaker, B. N., and D. J. Reddish (1989), *Subsidence: Occurrence, Prediction and Control*, Elsevier, Amsterdam, The Netherlands.

Wilson, C. J. N., and W. Hildreth (1997), The Bishop Tuff: New insights from eruptive stratigraphy, *J. Geol.*, *105*(4), 407–439.

Withjack, M. O., and C. Scheiner (1982), Fault patterns associated with domes—An experimental and analytical study, *Bull. Am. Assoc. Petroleum Geologists*, *66*(3), 302–316.

Yerkes, R. F., and R. O. Castle (1976), Seismicity and faulting attributable to fluid extraction, *Eng. Geol.*, *10*(2–4), 151–167.

Zuber, M. T., and P. J. Mouginis-Mark (1992), Caldera subsidence and magma chamber depth of the Olympus Mons Volcano, Mars, *J. Geophys. Res.*, *97*(E11), 18,295–18,307.